


# MULTI-BODY DYNAMIC MODELING OF A BIRD-LIKE FLAPPING-WING VEHICLE: ANALYSIS OF FLAPPING-AERODYNAMIC COUPLING EFFECTS

Libing Zhou[1,*], Bifeng Song[1,2], Yichi Liu[1], Mengxue Chen[3]& Qiang Fu[1,2]

[1]Northwestern Polytechnical University, Xi' an 710072, China
[2]National Key Laboratory of Aircraft Configuration Design, Xi' an 710072, China
[3]COMAC Shanghai Aircraft Manufacturing Co., Ltd., Shanghai 200123, China

## Abstract

This paper establishes a multi-body dynamic simulation framework integrated with a high-fidelity aerodynamic model for a bird-like flapping-wing vehicle named “Dove”. Surrogate models of wing-body combination for the cycle-average, instantaneous fluctuation, and damping part of aerodynamic forces and moments are developed based on wing-body wind tunnel experiments. Tail aerodynamic model is first estimated using vortex-lattice method, and then modified after full-set wind tunnel experiments. Newton–Euler method is used to establish a three-rigid-body dynamic model ($M_I$) describing symmetric flapping motion, and also a simplified single-body model ($S_I$) for comparative analysis. Simulation results of $M_I$ is able to capture the inertial coupling between flapping and rolling, and exhibits higher lateral-directional damping and faster convergence in disturbance and maneuver response. The results indicate significant differences between the $S_I$ and $M_I$, confirming the necessity of incorporating both multi-body dynamics and unsteady aerodynamics in modeling process.

**Keywords:** bird-like flapping-wing vehicle, multi-body dynamics, time-varying systems, Floquet analysis

## 1. Introduction

Bird-like flapping-wing vehicles (BFWVs) mimic the flight of natural birds, simultaneously generating both lift and thrust through wing flapping. Accurate calculation of the aerodynamic forces produced by the flapping wings under various flight conditions forms the foundation of dynamic simulation. Quasi-steady models based on empirical formulations [1 – 3] account for effects such as leading-edge vortices, rotational lift, viscosity, and added mass, providing functional expressions for lift and drag coefficients as functions of angle of attack. These models are widely used in flapping-wing aerodynamic modeling but suffer from low accuracy and are generally only suitable for rough modeling of rigid wings. Rapid aerodynamic estimation methods based on simplified theory represent a compromise between computational cost and accuracy, among which the most valuable are the modified strip theory [4 – 6] and the unsteady vortex-lattice method [7 – 10]. Additionally, surrogate models serve as effective tools for aerodynamic modeling. When constructing surrogate models, aerodynamic data can be pre-acquired at designed experimental state points through numerical computation or wind tunnel experiments, after which model training is conducted using response surface model, radial basis function, and other techniques [11 – 13], yielding relatively accurate aerodynamic models.

Meanwhile, since the tail is typically installed within the complex unsteady flow field generated by the flapping of the wings, studies have shown that wing-tail interference effects are particularly strong when the two are in close proximity, significantly affecting flapping efficiency, mean thrust [14], and the control forces and moments produced by the tail [15]. However, the flight speeds simulated or measured in the above studies are relatively low ($\leqslant$1 m/s), and further investigation is needed for fast forward flight of BFWVs.

https://doi.org/10.71945/icas2026_0191

The periodic flapping motion of the wings poses considerable challenges for dynamic modeling, and it is widely acknowledged that multi-rigid-body dynamic models are required to accurately characterize the dynamic behavior of flapping-wing vehicles [16,17]. The majority of existing multi-body dynamic models employ low-fidelity aerodynamic estimation models based on rigid-wing assumptions [18]; very few studies have considered wing flexibility [19], but due to model complexity constraints, the aerodynamic model is neglected. Loh et al. [20] developed a multi-body dynamic model for a hovering insect-like vehicle using experimentally derived aerodynamic data, but only considered the effects of cycle-averaged forces. Consequently, the simulation accuracy of existing multi-body models for BFWVs remains insufficient.

For birds and BFWVs with relatively low flapping frequencies, Taylor and Thomas [21] drew an analogy with fixed-wing longitudinal short/long-period mode characteristics, indicating that the short-period modal frequencies typically range from 0.15 to 1.5 Hz. The periodically varying aerodynamic forces can induce coupled body oscillations, rendering the cycle-averaging assumption invalid. Therefore, analysis of BFWV system characteristics often requires periodic stability analysis of the limit cycle at the trim condition. Dietl and Garcia [22] first applied Floquet theory to study the longitudinal stability of the linearized periodic time-varying open-loop system, revealing one unstable real eigenvalue, one stable real eigenvalue (analogous to a non-oscillatory short-period mode), and a pair of stable complex eigenvalues (analogous to the long-period mode). Shen et al. [23], combining untethered flight experiments, demonstrated through Floquet theory that the triple-rigid-body dynamic model of their designed BFWV was longitudinally and lateral-directionally stable in the open-loop condition, but exhibited a periodic flight state similar to spiral modal.

In view of the above, this paper undertakes the following work: (1) based on wind tunnel experimental data, a high-fidelity wing-body aerodynamic surrogate model that separates cycle-average and instantaneous fluctuation is constructed, and an estimation model for the damping part is established; (2) multi-rigid-body dynamic model is developed using Newton-Euler method, and trim limit cycles across the full flight envelope are numerically solved using the multiple shooting method; (3) through comparison of single-body and multi-body models, the effects of wing flapping motion are quantitatively analyzed. This study aims to reveal the coupling effects between flapping motion and unsteady aerodynamic forces, providing a more reliable model foundation for stability analysis and controller design of BFWVs.

## 2. Aerodynamic Modeling

This study takes the "Dove" BFWV as the platform [24], which has a maximum take-off weight of 256 g and a wingspan of 66 cm. The "Dove" currently employs an inverted T-tail configuration combining vertical and horizontal stabilizers with mixed elevator-aileron control, as illustrated in Figure 1.

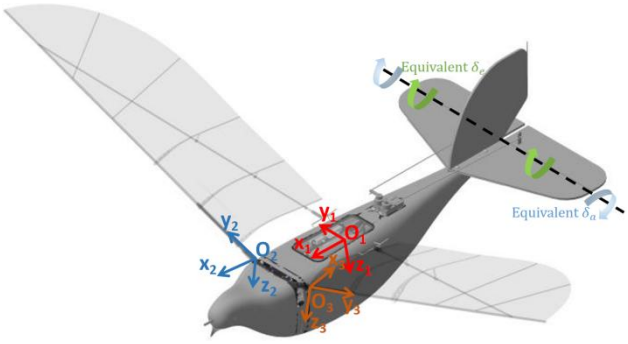



Figure 1 Demonstration of BFWV “Dove”

In this paper, the full-set aerodynamic model is divided into two parts: the wing-body model (subscript $bw$) and the tail model (subscript $t$), as shown in Equations 1 and 2. Due to the unsteady interference between the flapping wings and the fuselage, wind tunnel experiments are employed to establish surrogate models for the aerodynamic forces and moments of the "Dove" wing-body combination. Since the tail involves control surface deflections and thus requires aerodynamic data of various flight condition combinations, the vortex-lattice method is used for rapid primary

estimation of tail model, which is then modified using full-set wind tunnel experimental data.

$$\begin{bmatrix} L \\ T \\ Y \end{bmatrix} = \begin{bmatrix} L_{bw} + L_t \\ T_{bw} - D_t + T_t \\ L_{bw} + L_t \end{bmatrix} \tag{1}$$

$$\begin{bmatrix} M_x \\ M_y \\ M_z \end{bmatrix} = \begin{bmatrix} M_{x_{bw}} + M_{xt} \\ M_{y_{bw}} + M_{yt} \\ M_{z_{bw}} + M_{zt} \end{bmatrix} + \left( R_w^b \begin{bmatrix} L \\ T \\ Y \end{bmatrix} \right) \times \begin{bmatrix} -l_x \\ 0 \\ l_z \end{bmatrix} \tag{2}$$

## 2.1 Wing-Body Instantaneous Aerodynamic Model

The wind tunnel experimental system is shown in Figure 2. The test section has a circular cross-section of 1.6 m diameter, with turbulence intensity not exceeding 0.5%. The designed wind speed range is 5 to 15 m/s, covering the flight envelope of the "Dove" BFWV and meeting measurement accuracy requirements. A full-factorial experimental design approach was adopted to determine the wing-body model wind tunnel test conditions, with experimental factors being flapping frequency, freestream velocity, angle of attack, and sideslip angle. To establish a relatively accurate aerodynamic model using limited experimental state points, each experimental factor was selected to cover the full flight envelope of the "Dove" as far as the experimental apparatus permitted, as shown in Table 1.



Figure 2 Wind tunnel experiment of “Dove”

In this paper, the wing-body aerodynamic model is decomposed into the cycle-average ($\overline{\boldsymbol{F}}_{bw}$,$\overline{\boldsymbol{M}}_{bw}$), the instantaneous fluctuation ( $\widetilde{\boldsymbol{F}}_{bw}^{i}$ , $\widetilde{\boldsymbol{M}}_{bw}^{i}$ ), and the aerodynamic damping part ( $\boldsymbol{M}_{d}^{i}$ ), where aerodynamic forces are defined in the wind-axis system and aerodynamic moments are defined in the body-axis system. Dividing the instants within cycle ($i$) by the sampling frequency ($f_s$), we have:

$$i = \frac{tf_s}{Tf} (t < T) \tag{3}$$

where $f$ is the flapping frequency and $T$ is the flapping period. The aerodynamic force at the i-th instant within the cycle is:

$$F_{bw}^{i} = \overline{F}_{bw} + \widetilde{F}_{bw}^{i} \tag{4}$$

The aerodynamic moment at the i-th instant within the cycle is:

$$M_{bw}^{i} = \overline{M}_{bw} + \widetilde{M}_{bw}^{i} + M_{d}^{i} \tag{5}$$

Table 1 Selection of wind tunnel experimental state points.

| Experimental factor | Experimental value |
|---|---|
| Freestream velocity(V) | 8m/s、9m/s、10m/s、11m/s、12m/s |
| Flapping frequency(f) | 7Hz、8Hz、9Hz、10Hz |
| Angle of attack( α ) | -8°、-4°、0°、4°、8°、12°、16°、20° |
| Sideslip angle(β) | 0°、-2°、-4°、-6°、-8°、-10° |

### 2.1.1 Cycle-Average

For the cycle-averaged part, its relationship with the fitting independent variables $f$, V, α, β is primarily linear or quadratic. Wind tunnel data were collected for 1 s at each experimental state point and then cycle-averaged, yielding the following response surface model structures:

$$\overline{L}_{bw} \sim \Gamma_{\overline{L}}(1, \alpha, \alpha f, V\alpha, \alpha\beta, V^2\alpha, f, V, V^2, \beta) \tag{6}$$

$$\overline{T}_{bw} \sim \Gamma_{\overline{T}}(1, f, \alpha, \alpha^2, \beta, V, V^2) \tag{7}$$

$$\overline{Y}_{bw} \sim \Gamma_{\overline{Y}}(1, f, \alpha, \alpha^2, V, V^2)\beta \tag{8}$$

$$\overline{M_x}_{bw} \sim \Gamma_{\overline{M_x}}[(1, f, f^2, \alpha, V, V^2)\beta - (1, f, f^2, \alpha, V, V^2)sgn(\beta)\beta^2] \quad (9)$$

$$\overline{M_y}_{bw} \sim \Gamma_{\overline{M_y}}(1, \alpha, \alpha f, \alpha f^2, V\alpha, V^2\alpha, f, f^2V, V^2) \quad (10)$$

$$\overline{M_z}_{bw} \sim \Gamma_{\overline{M_z}}[(1, f, f^2, \alpha, V, V^2)\beta - (1, f, f^2, \alpha, V, V^2)sgn(\beta)\beta^2] \quad (11)$$

where $sgn(\beta) = \begin{cases} 1, & \beta > 0 \\ 0, & \beta = 0 \\ -1, & \beta < 0 \end{cases}$, and the regression results are shown in Figure 3(a). The correlation coefficients $R^2$ for longitudinal aerodynamic forces and moments all exceed 0.99, indicating high fitting accuracy. The lateral-directional aerodynamic moments are relatively small, while the side force magnitude is large with high fitting accuracy ($R^2 > 0.98$), providing accurate modeling of the dominant aerodynamic effects.

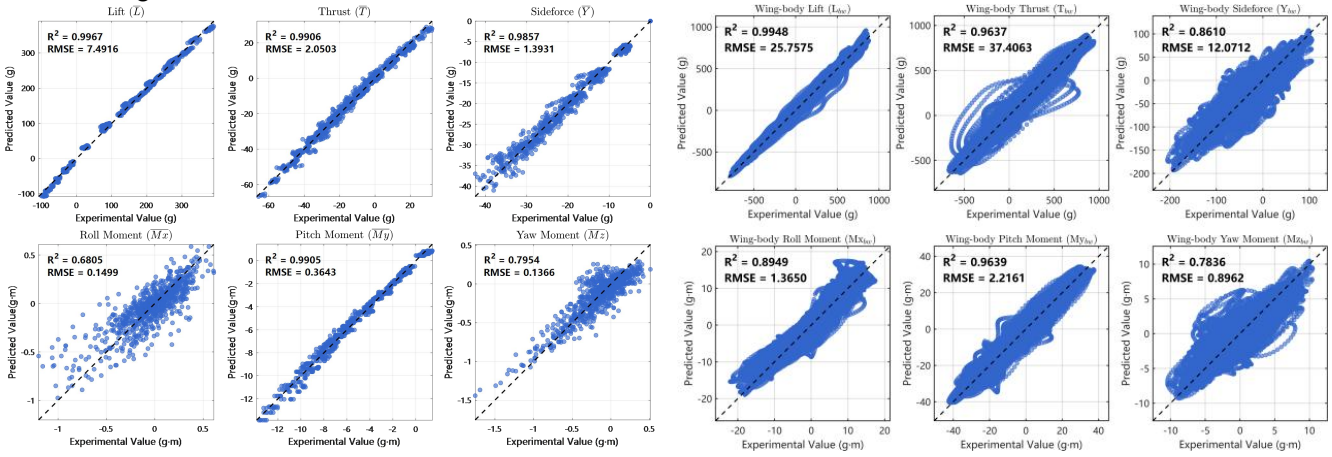
### 2.1.2 Instantaneous Fluctuation

Since the wind tunnel instantaneous data contain inertial forces generated by the flapping motion, the inertial forces must first be filtered out at each sampling point. As the "Dove" only performs symmetric flapping motion, the three-axis inertial moments in the body-axis system can be considered zero, with only the inertial force fluctuation ${}^{b}_{i}F$ along the body z-axis present, yielding:

$${}^{b}_{i}F = [0,0, b_{wg}m_w(\ddot{\delta}^2 sin\delta - \ddot{\delta}cos\delta)]^T \quad (12)$$

where $\delta$ is the flapping angle (positive upward), $m_w$ is the flapping-wing mass, and $b_{wg}$ is the spanwise position of the center of gravity of a single flapping wing.

For the instantaneous fluctuation, the instant of zero lift fluctuation ($\tilde{L}_{bw} = 0$) is selected as the cycle start point. After removing the inertial forces, a fully connected feedforward neural network is employed for fitting. The longitudinal hidden layers structure is 32×16, and the lateral-directional is 64×32. The inputs are $f$, $V$, $\alpha$, $\beta$, $i$. The decreasing structure is designed to hierarchically extract high-order features: the first layer captures local patterns, and the second layer performs feature integration. This design balances model capacity with overfitting risk. The fitting results are shown in Figure 3(b). The longitudinal correlation coefficients all exceed 0.96; the lateral-directional correlation coefficients all exceed 0.78, with small RMSE values, confirming the effectiveness of the surrogate model.




(a) (b)

Figure 3 Wing-body aerodynamic surrogate model fitting results for forces and moments: (a) cycle-average only; (b) including instantaneous fluctuation.

### 2.1.3 Aerodynamic Damping

Based on the established wing-body aerodynamic surrogate model, an estimation model for the wing-body damping effects is derived. Longitudinally, the primary effect is the pitch damping moment ($M^i_{yd}$) caused by the instantaneous angle-of-attack increment of the flapping wings due to pitch rate. Lateral-directionally, the primary effects are the roll and yaw damping moments ($M^i_{xd}$, $M^i_{zd}$) generated by the left/right flapping-wing velocity differences and sideslip angle increments arising from lateral velocity, roll rate, and yaw rate.

The instantaneous aerodynamic center position of the wing-body combination ($r_{cop}$) can be

estimated by:

$$r_{cop} = \frac{F_{bw} \times M_{bw}}{\|F_{bw}\|} + r_{exp} \tag{13}$$

where $r_{exp} = \begin{bmatrix} -l_x \\ 0 \\ l_z \end{bmatrix}$ is the wing-body wind tunnel experimental reference point. Then:

$$\begin{bmatrix} \Delta u \\ \Delta v \\ \Delta w \end{bmatrix} = \begin{bmatrix} p \\ q \\ r \end{bmatrix} \times r_{cop} \tag{14}$$

Thus the pitch moment damping can be estimated as:

$$\Delta\alpha = arctan\frac{u+\Delta u}{w+\Delta w} - arctan\frac{u}{w} \tag{15}$$

$$M_{yd}^{i} = [0 \quad \Delta\alpha \quad 0](r_{cop} \times (R_w^b \begin{bmatrix} \frac{\partial T_{bw}}{\partial \alpha} \\ 0 \\ -\frac{\partial L_{bw}}{\partial \alpha} \end{bmatrix})) \tag{16}$$

where $R_w^b$ is the transformation matrix from the wind-axis system to the body-axis system.

Similarly, the roll and yaw moments caused by the sideslip angle increment can be estimated as:

$$\Delta\beta = arcsin\frac{v+\Delta v}{V_\Delta} - arcsin\frac{v}{V} \tag{17}$$

$$\begin{bmatrix} M_{x\beta}^{i} \\ M_{z\beta}^{i} \end{bmatrix} = \begin{bmatrix} \Delta\beta & 0 & 0 \\ 0 & 0 & \Delta\beta \end{bmatrix} (r_{cop} \times (R_w^b \begin{bmatrix} \frac{\partial T_{bw}}{\partial \beta} \\ \frac{\partial Y_{bw}}{\partial \beta} \\ -\frac{\partial L_{bw}}{\partial \beta} \end{bmatrix})) \tag{18}$$

where $V$ is the current airspeed, $V_\Delta = \sqrt{(u+\Delta u)^2 + (v+\Delta v)^2 + (w+\Delta w)^2}$.

For symmetric flapping motion, the velocity at the pressure center of the flapping wing in the wind-axis system can be expressed as:

$$\overrightarrow{V_{cop}} = \begin{bmatrix} V - R_{cop}\dot{\delta}cos\delta sin\alpha \\ -R_{cop}\dot{\delta}sin\delta \\ -R_{cop}\dot{\delta}cos\delta cos\alpha \end{bmatrix} \tag{19}$$

where $R_{cop}$ is the spanwise position of the flapping-wing pressure center, typically taken at 60%–70% of the span length [25], and $\delta$ is the current flapping angle. The instantaneous lift and thrust coefficients can then be calculated as:

$$C_{Lbw} = \frac{L_{bw}}{\frac{1}{2}\rho V_{cop}^2 S_w} \tag{20}$$

$$C_{Tbw} = \frac{T_{bw}}{\frac{1}{2}\rho V_{cop}^2 S_w} \tag{21}$$

When roll and yaw angular rates are present, the left and right flapping-wing velocities are respectively:

$$\overrightarrow{V_l} = R_b^w \begin{bmatrix} -rR_{cop}cos\delta \\ [(p-\dot{\delta})R_{cop}]sin\delta + v \\ [(p-\dot{\delta})R_{cop}]cos\delta \end{bmatrix} + \begin{bmatrix} V \\ 0 \\ 0 \end{bmatrix} \tag{22}$$

$$\overrightarrow{V_r} = R_b^w \begin{bmatrix} rR_{cop}cos\delta \\ [(p+\dot{\delta})R_{cop}]sin\delta + v \\ [-(p+\dot{\delta})R_{cop}]cos\delta \end{bmatrix} + \begin{bmatrix} V \\ 0 \\ 0 \end{bmatrix} \tag{23}$$

Consequently, the lateral and directional damping components are:

$$M_{xd}^{i} = -\frac{1}{4}\rho(C_{Lbw}cos\alpha - C_{Tbw}sin\alpha)S_w R_{cop}(V_r^2 - V_l^2) + M_{x\beta}^{i} \tag{24}$$

$$M_{zd}^{i} = -\frac{1}{4}\rho(C_{Lbw}sin\alpha + C_{Tbw}cos\alpha)S_w R_{cop}(V_r^2 - V_l^2) + M_{z\beta}^{i} \tag{25}$$

## 2.2 Tail Aerodynamic Modeling

Following the classical aerodynamic derivative formulation for fixed-wing aircraft, the tail aerodynamic model is established as:

$$\begin{bmatrix} L_t \\ D_t \\ Y_t \end{bmatrix} = \frac{1}{2}\rho V^2 S_t \begin{bmatrix} C_{Lt} \\ C_{Dt} \\ C_{Yt} \end{bmatrix} \tag{26}$$

$$\begin{bmatrix} M_{xt} \\ M_{yt} \\ M_{zt} \end{bmatrix} = \frac{1}{2}\rho V^2 S_t \begin{bmatrix} b_t C_{lt} \\ c_t C_{mt} \\ b_t C_{nt} \end{bmatrix} \tag{27}$$

$$C_{Lt} = C_{Lt0} + C_{Lt\alpha}\alpha + C_{Lt\delta_e}\delta_e \tag{28}$$

$$C_{Dt} = C_{Dt0}(\delta_e) + kC_{Lt}^2 \tag{29}$$

$$C_{Yt} = C_{Y\beta}(\alpha)\beta \tag{30}$$

$$C_{lt} = C_{l\beta}(\alpha)\beta + C_{lpt}\frac{b_t}{2V}p + C_{lrt}\frac{b_t}{2V}r + C_{lt\delta_a}\delta_a \tag{31}$$

$$C_{mt} = C_{mt0} + C_{mt\alpha}\alpha + C_{mt\delta_e}\delta_e + C_{mqt}\frac{c_t}{2V}q \tag{32}$$

$$C_{nt} = C_{n\beta}(\alpha)\beta + C_{npt}\frac{b_t}{2V}p + C_{nrt}\frac{b_t}{2V}r + C_{nt\delta_a}\delta_a \tag{33}$$

where the aerodynamic coefficients of tail are estimated using the vortex-lattice method. $C_{Y\beta}(\alpha)$, $C_{l\beta}(\alpha)$, $C_{n\beta}(\alpha)$ are fitted using second-order polynomials of $\alpha$ based on aerodynamic data.

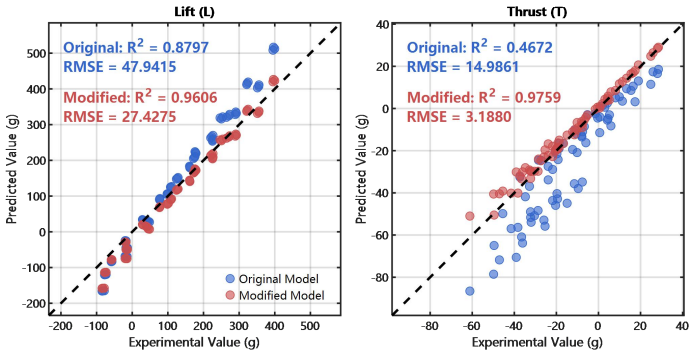



Figure 4 Full-aircraft aerodynamic model correction results.

## 2.3 Wing-Tail Interference Modification

Similar to fixed-wing aircraft, the wake generated by the flapping wings also exhibits a certain downwash effect. Therefore, this paper estimates the downwash angle of the flapping-wing wake at low speeds based on classical lifting-line theory. In actual flight, the interference between the flapping wings and the tail is more complex. After the uniform freestream passes through the flapping plane, the up-and-down flapping motion of the wings and the torsional deformation of the flexible wings produce a rearward compression effect similar to that of a propeller, resulting in a partial thrust effect on the tail.

Full-set wind tunnel tests were conducted on the "Dove" with flapping frequency of 7~9 Hz, angle of attack of −8°~20°, and freestream velocity V of 8~12 m/s. A response surface model was developed for the thrust gained by the tail. The model form was determined by p-value testing as:

$$T_t = c_0 + c_V V + c_f f + c_{V^2}V^2 + c_{aV}\alpha V + c_{\alpha^2}\alpha^2 + c_{Vf}Vf \tag{34}$$

The coefficient values determined by least squares are shown in Table 2.

Table 2 Response surface modeling coefficients for thrust gained by the tail.

| $c_0$ | $c_V$ | $c_f$ | $c_{V^2}$ | $c_{aV}$ | $c_{\alpha^2}$ | $c_{Vf}$ |
|---|---|---|---|---|---|---|
| 180.6202 | -48.2589 | 7.5023 | 2.7823 | 0.0402 | -0.0177 | -0.4273 |

The correlation coefficient $R^2$ was computed for both the modified and unmodified models against the wind tunnel experimental results, as shown in Figure 4. The results show that the model with wing-tail interference modification achieves further improvement in correlation coefficients, demonstrating higher accuracy.

# 3. Dynamic Simulation and Analysis Methods

## 3.1 Six-DOF Triple-Rigid-Body Dynamic Equations

The flapping wings of the "Dove" have relatively low mass, accounting for approximately 6.2% of the total weight, with no active twist or sweep during flapping, consistent left/right flapping

frequency, and relatively simple flapping kinematics. Moreover, since the flapping frequency is prescribed as a real-time system input at each instant, this paper adopts the Newton–Euler method to establish a left-wing–fuselage–right-wing triple-rigid-body dynamic model of the "Dove", as illustrated in Figure 1. Under the prescribed flapping kinematics, the six-degree-of-freedom response of the fuselage is simulated and compared with that of a single-rigid-body model to analyze the effects of wing flapping.

The fuselage and tail are designated as rigid body 1, the left wing as rigid body 2, and the right wing as rigid body 3. The origin of the fuselage coordinate system is fixed at the aircraft center of gravity; the origin of the left-wing coordinate system is fixed at the hinge point between the fuselage and the left flapping wing; and the origin of the right-wing coordinate system is fixed at the hinge point between the fuselage and the right flapping wing. Expressed in each local coordinate system, we have:

$$\begin{matrix} F_i = m_i a_i + \omega_i \times (m_i v_i) \\ M_i = J_i \beta_i + \omega_i \times (J_i \omega_i) \end{matrix}, \quad i = 1,2,3 \tag{35}$$

where $F_i$ is the resultant external force acting on rigid body i expressed in the i-frame, $a_i$ is the acceleration of rigid body i expressed in the i-frame, $\beta_i$ is the angular acceleration of rigid body i expressed in the i-frame, $M_i$ is the resultant external moment acting on rigid body i expressed in the i-frame, $m_i$ is the mass diagonal matrix of rigid body i, $J_i$ is the inertia tensor matrix of rigid body i in the i-frame, $\omega_i$ is the three-axis angular velocity vector of rigid body i, and $v_i$ is the three-axis velocity vector of rigid body i.

Since the flapping wings are single-degree-of-freedom in flapping form, the angular velocities of the left and right wings relative to the fuselage are:

$${}^2_1\omega = \begin{bmatrix} \dot{\delta} \\ 0 \\ 0 \end{bmatrix}, {}^2_1\beta = \begin{bmatrix} \ddot{\delta} \\ 0 \\ 0 \end{bmatrix}, {}^3_1\omega = \begin{bmatrix} -\dot{\delta} \\ 0 \\ 0 \end{bmatrix}, {}^3_1\beta = \begin{bmatrix} -\ddot{\delta} \\ 0 \\ 0 \end{bmatrix} \tag{36}$$

The velocities, accelerations, angular velocities, and angular accelerations of the left and right wings ($i = 2,3$) are:

$$v_i = |{}^i_1O|_\times {}^i_1R\omega_1 + {}^i_1Rv_1 \tag{37}$$
$$a_i = |{}^i_1O|_\times {}^i_1R\beta_1 + {}^i_1Ra_1 + v_i \times {}^i_1\omega \tag{38}$$
$$\omega_i = {}^i_1R\omega_1 + {}^i_1\omega \tag{39}$$
$$\beta_i = {}^i_1R\beta_1 + \omega_i \times {}^i_1\omega + {}^i_1\beta \tag{40}$$

where ${}^i_1R$ is the coordinate transformation matrix from frame 1 to frame i, and $|{}^i_1O|_\times$ is the skew-symmetric form of the coordinates of the origin of frame 1 in frame i. Denoting:

$${}^i_jX = \begin{bmatrix} {}^i_jR & 0 \\ |{}^i_jO|_\times {}^i_jR & {}^i_jR \end{bmatrix}, \quad {}^i_jX^* = \begin{bmatrix} {}^i_jR & |{}^i_jO|_\times {}^i_jR \\ 0 & {}^i_jR \end{bmatrix} \tag{41}$$

By defining the following vector multiplication:

$$\begin{bmatrix} \overrightarrow{a_1} \\ \overrightarrow{a_2} \end{bmatrix} \times \begin{bmatrix} \overrightarrow{b_1} \\ \overrightarrow{b_2} \end{bmatrix} = \begin{bmatrix} \overrightarrow{a_1} \times \overrightarrow{b_1} \\ \overrightarrow{a_2} \times \overrightarrow{b_1} + \overrightarrow{a_1} \times \overrightarrow{b_2} \end{bmatrix}, \quad \begin{bmatrix} \overrightarrow{a_1} \\ \overrightarrow{a_2} \end{bmatrix} \times^* \begin{bmatrix} \overrightarrow{b_1} \\ \overrightarrow{b_2} \end{bmatrix} = \begin{bmatrix} \overrightarrow{a_1} \times \overrightarrow{b_1} + \overrightarrow{a_2} \times \overrightarrow{b_2} \\ \overrightarrow{a_1} \times \overrightarrow{b_2} \end{bmatrix} \tag{42}$$

Equations (35)~(40) can be expressed in matrix form as:

$${}^1_1W = {}^1_1I\,{}^1_1A + {}^1_1V \times^* \left({}^1_1I\,{}^1_1V\right) \tag{43}$$
$${}^2_2W = {}^2_2I\,{}^2_2A + {}^2_2V \times^* \left({}^2_2I\,{}^2_2V\right) \tag{44}$$
$${}^3_3W = {}^3_3I\,{}^3_3A + {}^3_3V \times^* \left({}^3_3I\,{}^3_3V\right) \tag{45}$$
$${}^2_2V = {}^2_1X\,{}^1_1V + {}^2_2S\dot{\delta} \tag{46}$$
$${}^2_2A = {}^2_1X\,{}^1_1A + {}^2_2V \times {}^2_2S\dot{\delta} + {}^2_2S\ddot{\delta} \tag{47}$$
$${}^3_3V = {}^3_1X\,{}^1_1V + {}^3_3S\dot{\delta} \tag{48}$$
$${}^3_3A = {}^3_1X\,{}^1_1A + {}^3_3V \times {}^3_3S\dot{\delta} + {}^3_3S\ddot{\delta} \tag{49}$$

where ${}^i_iW = \begin{bmatrix} M_i \\ F_i \end{bmatrix}$, ${}^i_iV = \begin{bmatrix} \omega_i \\ v_i \end{bmatrix}$, ${}^i_iI = \begin{bmatrix} J_i & 0 \\ 0 & m_i \end{bmatrix}$, ${}^i_iA = \begin{bmatrix} \beta_i \\ a_i \end{bmatrix}$, ${}^2_2S = \begin{bmatrix} 1 \\ 0 \\ 0 \\ 0 \\ 0 \\ 0 \end{bmatrix}$, ${}^3_3S = \begin{bmatrix} -1 \\ 0 \\ 0 \\ 0 \\ 0 \\ 0 \end{bmatrix}$.

Summing the resultant external forces and moments of each part expressed in frame 1 through coordinate transformation, the interaction forces between the fuselage and the left/right wings cancel out. At this point, the left-hand side of the equation represents the total external force (sum of aerodynamic force and gravity) and total external moment (aerodynamic moment) of the entire vehicle. Substituting the acceleration transformation yields:

$$\begin{bmatrix} M_{aero} \\ F_{aero} + G \end{bmatrix} = \left({}^{1}_{1}I + {}^{1}_{2}X^{*}\,{}^{2}_{2}I\,{}^{2}_{1}X + {}^{1}_{3}X^{*}\,{}^{3}_{3}I\,{}^{3}_{1}X\right){}^{1}_{1}A + {}^{1}_{1}V\times^{*}\left({}^{1}_{1}I\,{}^{1}_{1}V\right) + {}^{1}_{2}X^{*}({}^{2}_{2}V\times^{*}\left({}^{2}_{2}I\,{}^{2}_{2}V\right)) + {}^{1}_{2}X^{*}\,{}^{2}_{2}I({}^{2}_{2}V \times {}^{2}_{2}S\dot{\delta} + {}^{2}_{2}S\ddot{\delta}) + {}^{1}_{3}X^{*}({}^{3}_{3}V\times^{*}\left({}^{3}_{3}I\,{}^{3}_{3}V\right)) + {}^{1}_{3}X^{*}\,{}^{3}_{3}I({}^{3}_{3}V \times {}^{3}_{3}S\dot{\delta} + {}^{3}_{3}S\ddot{\delta}) \quad (50)$$

With real-time aerodynamic model inputs, the above equation can be solved for ${}^{1}_{1}A$, thereby realizing the solution of the triple-rigid-body dynamic equations for the BFWV. When the mass contribution of the flapping wings is neglected, the above equations reduce to the following single-rigid-body dynamic equations:

$$\begin{bmatrix} M_{aero} \\ F_{aero} + G \end{bmatrix} = {}^{1}_{1}I\,{}^{1}_{1}A + {}^{1}_{1}V\times^{*}\left({}^{1}_{1}I\,{}^{1}_{1}V\right) \quad (51)$$

where ${}^{1}_{1}I$ in this case represents the total mass and inertia matrix expressed in the body-axis system.

## 3.2 Trim Flight Condition Search

Under the influence of periodically time-varying aerodynamic forces, the trim condition of the BFWV exists in the form of a limit cycle. Due to the high complexity and nonlinearity of the dynamic and aerodynamic models, an analytical solution for the limit cycle is essentially impossible to obtain. Therefore, this paper employs the multiple shooting method to numerically search for trim initial states—including angle of attack, sideslip angle, Euler angles, control surface deflection angles, and three-axis velocities, thereby obtaining limit cycles at different flapping frequencies.

The essence of the multiple shooting method is to divide the limit cycle into N sub-instants and impose constraints on the variables to be trimmed at each node, thereby accelerating the search. The external system inputs are flapping frequency $f_{trim}$, equivalent elevator deflection $\delta_{e_{trim}}$, and equivalent aileron deflection $\delta_{a_{trim}}$, all maintained at fixed values in the trim condition. Consequently, the limit cycle period is determined by the flapping frequency, which facilitates the trim search and better reflects actual flight conditions. At the i-th instant of the limit cycle, the state variables with periodicity are:

$$\mathrm{x_i} = [q\ \theta\ u\ w\ p\ r\ v\ \phi\ \psi]^{\mathrm{T}} \quad (52)$$

The selection of state variables is not unique. Here the longitudinal states include the pitch angular rate, pitch angle, forward and vertical velocity in the body-axis system, and the lateral-directional states include the roll rate, yaw rate, lateral velocity, roll and yaw angle in the body-axis system.

From the state transition, we have:

$$x_{i+1} = G(x_i, u_{trim}, t_i),\ \ 1 \le i \le N-1 \quad (53)$$

where $u_{trim} = [f_{trim}\ \delta_{e_{trim}}\ \delta_{a_{trim}}]^T$, and $G$ represents the state transition mapping determined by the single/multi-body dynamic equations. The periodicity requirement of the limit cycle yields:

$$x_1 = G(x_N, u_{trim}, t_N) \quad (54)$$

For different trimmed flight conditions, additional constraints can be imposed. For example, when solving for a constant-altitude level flight condition:

$$h_{i+1} = G_h(x_i, h_i),\ \ 1 \le i \le N-1 \quad (55)$$

$$h_1 = G_h(x_N, h_N) \quad (56)$$

$$\phi_i = 0,\ \ \forall i \in [1, N] \quad (57)$$

Multiple limit cycles may exist within the flight envelope of the flapping-wing vehicle. To constrain the obtained limit cycle, an average velocity for the resulting limit cycle is typically specified. Thus, the trim search can be transformed into a multivariate nonlinearly constrained optimization problem. For instance, solving for a level-flight limit cycle at a given trim speed $V_{trim}$ can be formulated as:

$$\min_X f(X) = \bar{V}_i - V_{trim}$$

$$s.t.\begin{cases} x_{i+1} - G(x_i, u_{trim}, t_i) = 0, 1 \le i \le N-1 \\ x_1 = G(x_N, u_{trim}, t_N) \\ h_{i+1} = G_h(x_i, h_i), 1 \le i \le N-1 \\ h_1 = G_h(x_N, h_N) \\ \phi_i = 0, \forall i \in [1, N] \end{cases} \tag{58}$$

where $X = [x_1^T \quad \cdots \quad x_N^T]^T$. For such large-scale optimization problems with numerous variables and nonlinear constraints, this paper adopts an interior-point optimization algorithm based on step decomposition for the solution.

### 3.3 Trim Modal Analysis Method

Based on the trim limit cycles obtained, Floquet theory is employed for modal characteristic analysis, with the system modal values used to assess dynamic stability. For the N sub-instants within the obtained limit cycle, the complete system is linearized at each instant, yielding the linear state-space matrices:

$$A_i = \frac{\partial G(x_i, u_{trim}, t_i)}{\partial x_i} \tag{59}$$

$$B_i = \frac{\partial G(x_i, u_{trim}, t_i)}{\partial u_{trim}} \tag{60}$$

Using a zero-order hold for discretization:

$$\Phi_i = e^{A_i T_s} \tag{61}$$

where $T_s$ is the sampling period, and $\Phi_i$ represents the system transition matrix from instant i to instant i+1.

The Floquet matrix is defined as $\Phi_T = \prod_{i=1}^{N} \Phi_i$, representing the perturbation state transition over one trim period. Its eigenvalues, i.e., the Floquet multipliers, determine the stability of the periodic orbit.

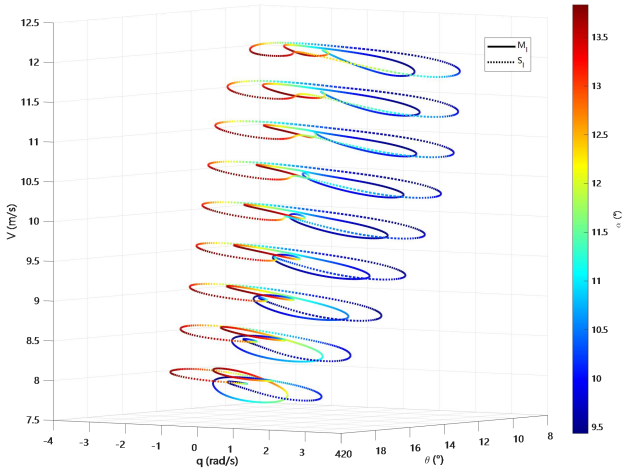



Figure 5 Comparison of limit cycles under steady level flight with the instantaneous aerodynamic model.

## 4. Results and Analysis

This section compares the time-varying single-body model ($S_1$) and the time-varying multi-body model ($M_1$) of the "Dove". Trim conditions are primarily selected for level flight and circling flight; non-trim responses are based on perturbations or maneuvers applied from the level-flight steady state.

### 4.1 Trim Characteristics Comparison

The limit cycles at various speeds are compared in Figure 5. Comparing the single-body and multi-body models reveals that, although the cycle-averaged values of angle of attack and pitch angle are nearly identical, differences exist in fluctuations within cycle. The longitudinal pitch oscillation amplitude of the multi-body model is noticeably smaller than that of the single-body model, indicating that neglecting the flapping motion of the wings amplifies the estimated instantaneous oscillations of the entire vehicle.

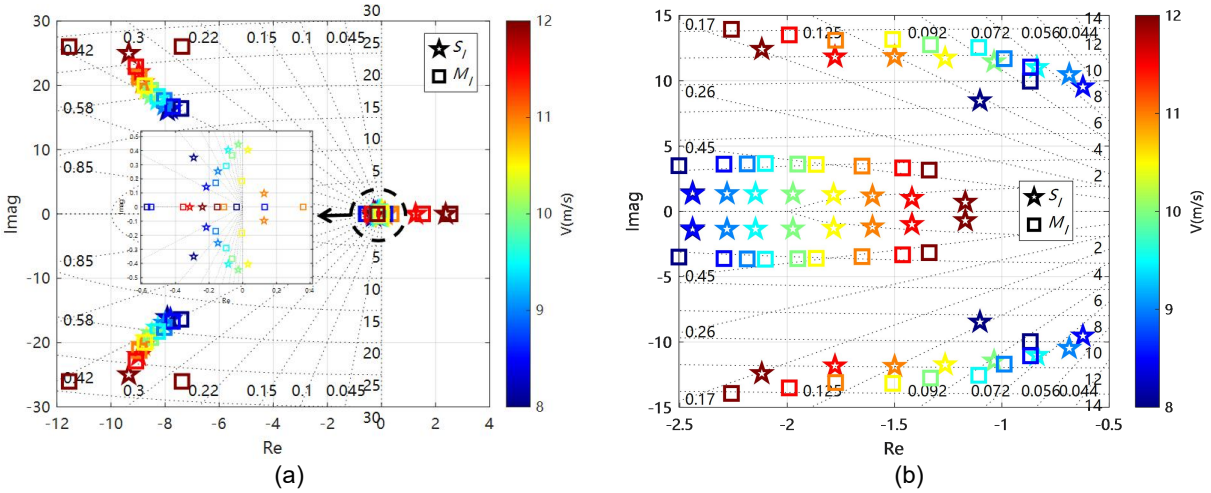



Figure 6 Comparison of modal characteristics for steady level flight: (a) longitudinal; (b) lateral-directional.

The Floquet multipliers for level-flight modes of the single-body and multi-body models are shown in Figure 6(a), with the discrete modes already transformed to the continuous domain using a zero-order hold. For the longitudinal modal characteristics, both models tend toward instability as the flight speed increases. One pair of complex roots obtained from Floquet decomposition is analogous to the short-period mode; the single-body and multi-body models exhibit consistent trends with speed and similar damping ratios. The simplified modal response manifests as rapid convergence dominated by pitch angular rate, as shown in Figure 7(b), with both models showing essentially identical behavior. The other pair of complex roots is analogous to the long-period mode, dominated by slow oscillatory convergence of the forward speed u, as shown in Figure 7(a). The single-body model exhibits a noticeably smaller damping ratio and slower convergence.

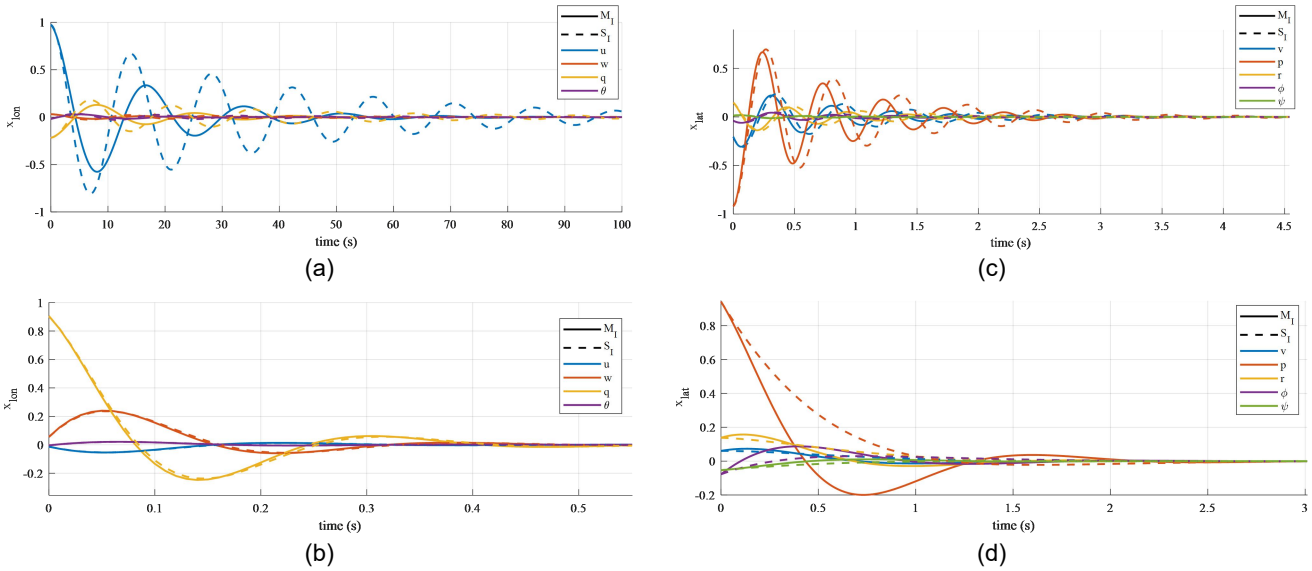



Figure 7 Comparison of simplified modal theoretical excitation responses (V = 10 m/s example): (a) longitudinal short-period-like mode; (b) longitudinal long-period-like mode; (c) lateral-directional Dutch-roll-like mode; (d) lateral-directional roll-convergence-like mode.

The lateral-directional modal characteristics for level flight are shown in Figure 6(b). Both the single-body and multi-body models are stable at all speeds. One pair of complex roots from Floquet decomposition yields a simplified modal response characterized by rapid convergence dominated by roll rate, as shown in Figure 7(d). The convergence rates of the two models are similar, with the single-body model having a larger damping ratio. The other pair of poles has a significantly higher natural frequency and noticeably smaller damping ratio, exhibiting multiple-oscillation convergence, as shown in Figure 7(c). The single-body model($S_I$) has a slightly lower frequency, and its damping ratio is excessively large at low speeds.

Based on typical flight profile requirements, the trim control surface deflections required for level

flight and steady circling at an average roll angle of 30° were calculated, as shown in Figure 8. The single-body and multi-body models are very close in level flight, while deviations are somewhat larger in circling at low and high speed ranges. The multi-body model($M_I$) indicates that the roll control performance of the "Dove" deteriorates significantly at low speeds, with the required $\delta_{a_{trim}}$ at 8 m/s approaching −15°, far exceeding the −3.42° predicted by the single-body model($S_I$). This is due to the inertial coupling between the flapping motion and the whole body rolling motion, which generates a non-zero mean rolling inertial moment. The increase in $\delta_{a_{trim}}$ required for the multi-body model directly reflects the mean inertial disturbance introduced by the flapping motion, which should not be ignored for maneuver analysis at low speeds.

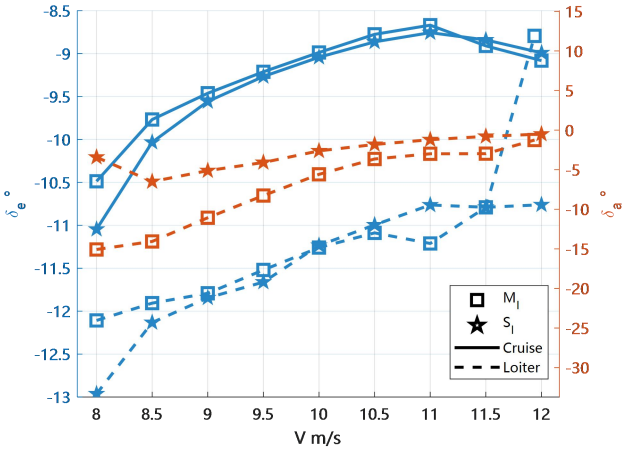
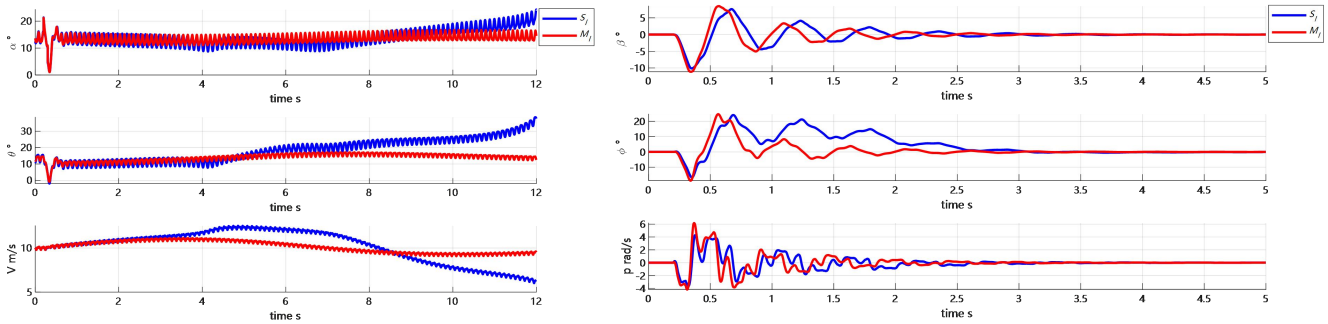



Figure 8 Required control surface deflections for trim with the original tail.

## 4.2 Instantaneous Response Comparison

### 4.2.1 Disturbance Response

Based on the 10 m/s trim condition, a 0.1 rad step change in angle of attack lasting 0.1 s is applied at 0.2 s. The longitudinal system response is shown in Figure 9(a). The response of the single-body model( $S_I$ ) diverges after 8 s, failing to maintain stability, which contradicts the modal characteristics. It can be observed that, although the modal characteristics are similar, the transient dynamic response is significantly affected by the coupling of single/multi-body dynamics and unsteady aerodynamics. The disturbance response of the multi-body model is essentially consistent with the modal characteristics, confirming that the simplified modes based on Floquet theory provide a reasonable assessment of the system characteristics.




(a) (b)

Figure 9 Comparison of disturbance responses (V = 10 m/s example): (a) angle-of-attack disturbance (0.1 rad, 0.1 s duration); (b) sideslipt disturbance (0.1 rad, 0.1 s duration).

Based on the 10 m/s trim condition, a 0.1 rad step change in sideslip angle lasting 0.1 s is applied at 0.2 s. The lateral-directional system response is shown in Figure 9(b). All model responses converge, and the multi-body model($M_I$) converges faster, indicating that the flapping motion can increase equivalent lateral-directional damping, thereby accelerating convergence.

### 4.2.2 Maneuver Response

A 1° elevator deflection( $\delta_e$) is applied, causing the vehicle to pitch down, as shown in Figure 10(a). The multi-body model($M_I$) produces an angle-of-attack change of approximately 7°, slightly larger

than that of the single-body model($S_1$). The pitch angle reaches a steady state after two periodic oscillations, exhibiting relatively poor dynamic characteristics. Overall, the longitudinal maneuver responses of the two models are similar.

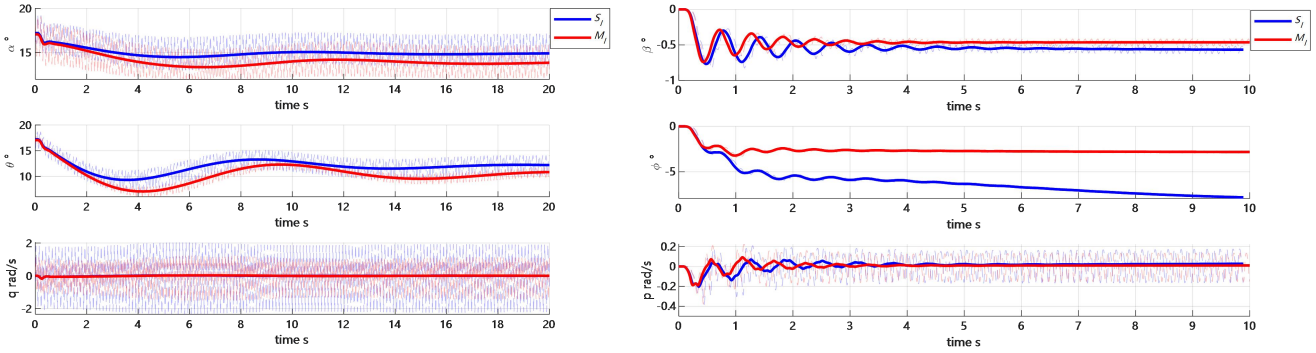



Figure 10 Comparison of maneuver responses, instantaneous response shown with 30% transparency dashed lines, mean value represented by solid lines: (a) equivalent elevator( $\delta_e$) step; (b) equivalent aileron( $\delta_a$) step.

Applying a 1° aileron deflection( $\delta_a$) causes the vehicle to enter a left turn, as shown in Figure 10(b). The multi-body model($M_1$) can establish a steady turn, whereas the single-body model($S_1$) fails to maintain stability, demonstrating that the single-body model($S_1$) is inaccurate for simulating lateral-directional responses. The steady-state roll angle change of the multi-body model is approximately −2.7°, indicating relatively weak lateral-directional maneuverability of the "Dove".

## 5. Conclusions and Discussion

This paper employs response surface fitting and shallow neural networks to establish a high-fidelity wing-body aerodynamic surrogate model based on wind tunnel data. An estimation model for aerodynamic damping is developed, and the partial thrust effect of tail is quantified. Combined with the multiple shooting method, the trim limit cycles for multi-rigid-body dynamic simulation are solved. Through model comparison, the intra-cycle dynamic characteristics resulting from flapping motion and unsteady aerodynamic coupling are verified. The influence of flapping motion on modal characteristics is relatively minor; however, it is still observed that flapping motion significantly accelerates the longitudinal long-period convergence rate, leading to stable convergence of the multi-body model in disturbance response. The lateral-directional characteristics are primarily influenced by the high-frequency complex roots, with flapping introducing additional equivalent aerodynamic damping that accelerates oscillatory convergence. At the same time, the effect of the mean inertial disturbance introduced by the flapping motion becomes more significant at low speeds, resulting in poor roll control for the flapping-wing vehicle employing mixed elevator-aileron control at low flight speeds. All of the above differences confirm that, when coupled with unsteady aerodynamics, the dynamic characteristics of the flapping-wing vehicle can be significantly altered by whether considering the dynamic effects of flapping motion, which should not be neglected even with the flapping-wing mass comprising only 6.2% of the total. Based on the dynamic simulation framework established in this paper, future work will develop controllers that account for flapping effects to achieve efficient control, while also exploring improvements to roll control mechanisms to enhance roll capability at low speeds.

## 6. Contact Author Email Address

*Corresponding author: august.823@mail.nwpu.edu.cn

## 7. Copyright Statement

The authors confirm that they, and/or their company or organization, hold copyright on all of the original material included in this paper. The authors also confirm that they have obtained permission, from the copyright holder of any third party material included in this paper, to publish it as part of their paper. The authors confirm that they give permission, or have obtained permission from the copyright holder of this paper, for the publication and distribution of this paper as part of the ICAS proceedings or as individual off-prints from the proceedings.

## References


[1] Andersen A, Pesavento U, Wang Z J. Unsteady aerodynamics of fluttering and tumbling plates[J]. Journal of Fluid Mechanics, 2005, 541(1): 65.

[2] Dickinson M H, Götz K G. Unsteady Aerodynamic Performance of Model Wings at Low Reynolds Numbers[J]. Journal of Experimental Biology, 1993, 174(1): 45-64.

[3] Pesavento U, Wang Z J. Falling Paper: Navier-Stokes Solutions, Model of Fluid Forces, and Center of Mass Elevation[J]. Physical Review Letters, 2004, 93(14): 144501.

[4] Lee J S, Kim D K, Lee J Y, et al. Experimental evaluation of a flapping-wing aerodynamic model for MAV applications[C]. Ahmadian M. The 15th International Symposium on: Smart Structures and Materials & Nondestructive Evaluation and Health Monitoring. San Diego, California, 2008: 69282M.

[5] DeLaurier J D. An aerodynamic model for flapping-wing flight[J]. The Aeronautical Journal, 1993, 97(964): 125-130.

[6] Kim D K, Lee J S, Han J H. Improved Aerodynamic Model for Efficient Analysis of Flapping-Wing Flight[J]. AIAA Journal, 2011, 49(4): 868-872.

[7] Savastano E, Perez-Sanchez V, Arrue B C, et al. High-Performance Morphing Wing for Large-Scale Bio-Inspired Unmanned Aerial Vehicles[J]. IEEE Robotics and Automation Letters, 2022, 7(3): 8076-8083.

[8] Long L N, Fritz T E. Object-Oriented Unsteady Vortex Lattice Method for Flapping Flight[J]. Journal of Aircraft, 2004, 41(6): 1275-1290.

[9] Ghommem M, Collier N, Niemi A H, et al. On the shape optimization of flapping wings and their performance analysis[J]. Aerospace Science and Technology, 2014, 32(1): 274-292.

[10] Lambert T, Abdul Razak N, Dimitriadis G. Vortex Lattice Simulations of Attached and Separated Flows around Flapping Wings[J]. Aerospace, 2017, 4(2): 22.

[11] Trizila P, Kang C kwon, Visbal M, et al. A Surrogate Model Approach in 2-D Versus 3-D Flapping Wing Aerodynamic Analysis[C]. 12th AIAA/ISSMO Multidisciplinary Analysis and Optimization Conference. Victoria, British Columbia, Canada: American Institute of Aeronautics and Astronautics, 2008.

[12] Bhosekar A, Ierapetritou M. Advances in surrogate based modeling, feasibility analysis, and optimization: A review[J]. Computers & Chemical Engineering, 2018, 108: 250-267.

[13] Nian P, Song B, Xuan J, et al. A Wind Tunnel Experimental Study on the Flexible Flapping Wing With an Attached Airfoil to the Root[J]. IEEE Access, 2019, 7: 47891-47903.

[14] Tay W B, Bijl H, Van Oudheusden B W. Biplane and Tail Effects in Flapping Flight[J]. AIAA Journal, 2013, 51(9): 2133-2146.

[15] Armanini S, Caetano J, De Visser C, et al. Modelling wing wake and tail aerodynamics of a flapping-wing micro aerial vehicle[J]. International Journal of Micro Air Vehicles, 2019, 11: 175682931983367.

[16] Gebert G, Gallmeier P, Evers J. Equations of Motion for Flapping Flight[C]//AIAA Atmospheric Flight Mechanics Conference and Exhibit. Monterey, California: American Institute of Aeronautics and Astronautics, 2002.

[17] Orlowski C T, Girard A R. Modeling and Simulation of Nonlinear Dynamics of Flapping Wing Micro Air Vehicles[J]. AIAA Journal, 2011, 49(5): 969-981.

[18] Xue D., Zhu Z., Song B.,etal. A review of key technologies of bird inspired flapping-wing micro aerial vehicles. Acta Aeronautica et Astronautica Sinica, 45(22):029984, 2024.

[19] Jahanbin Z, Selk Ghafari A, Ebrahimi A, et al. Multi-body simulation of a flapping-wing robot using an efficient dynamical model[J]. Journal of the Brazilian Society of Mechanical Sciences and Engineering, 2016, 38(1): 133-149.

[20] Loh K H, Cook M. Flight Dynamic Modelling and Control System Design for a Flapping Wing Micro Aerial Vehicle at Hover[C]. AIAA Atmospheric Flight Mechanics Conference and Exhibit. Austin, Texas: American Institute of Aeronautics and Astronautics, 2003.

[21] Taylor G K, Thomas A L R. Animal Flight Dynamics II. Longitudinal Stability in Flapping Flight[J]. Journal of Theoretical Biology, 2002, 214(3): 351-370.

[22] Dietl J M, Garcia E. Stability in Ornithopter Longitudinal Flight Dynamics[J]. Journal of Guidance, Control, and Dynamics, 2008, 31(4): 1157-1163.

[23] Shen Y, Ge W, Miao P. Multibody-Dynamic Modeling and Stability Analysis for a Bird-scale Flapping-wing Aerial Vehicle[J]. Journal of Intelligent & Robotic Systems, 2021, 103(1): 9.

[24] Yang W, Wang L, Song B. Dove: A biomimetic flapping-wing micro air vehicle[J]. International Journal of Micro Air Vehicles, 2018, 10(1): 70-84.

[25] Xinyan Deng, Schenato L, Wei Chung Wu, et al. Flapping flight for biomimetic robotic insects: part I-system modeling[J]. IEEE Transactions on Robotics, 2006, 22(4): 776-788.